Binocular Structured Light 3-D Reconstruction System for Low-Light Underwater Environments: Design, Modeling, and Laser-Based Calibration

Yaming Ou, Junfeng Fan, *Member, IEEE*, Chao Zhou, *Member, IEEE*, Shifei Tian, Long Cheng, *Senior Member, IEEE*, and Min Tan

Abstract— The 3-D perception of the low-light underwater environment has always been a major challenge, which greatly limits underwater operations. In this article, an underwater active vision measurement system based on binocular structured light is designed to achieve high-precision 3-D reconstruction. First, the fusion technology of binocular camera and laser addresses underwater optical attenuation and feature sparsity. Then, in order to avoid the huge inertia caused by the overall movement of the system, a laser scanner based on the mirror galvanometer is used to accomplish static scanning of the scene. Subsequently, considering the influence of multiple media, underwater refraction models, including the monocular imaging model, the binocular ranging model, and the binocular polar curve constraint model, are systematically proposed. What is more, the conventional checkerboard-based passive visual calibration method is ineffective for low-light waters. Therefore, a simple calibration block is designed, and a new multiobjective laser-based calibration algorithm based on laser geometric constraints is proposed. Finally, the effectiveness of the system is verified by analyzing the 3-D reconstruction results of underwater objects.

Index Terms— Binocular structured light, laser scanning, laser-based calibration, underwater 3-D reconstruction, underwater active vision.

I. INTRODUCTION

OVER the years, the rapid development of underwater robotic platforms, such as a remote operated vehicle

(ROV) [1], autonomous underwater vehicle (AUV) [2], and bionic robotic fish [3], has greatly facilitated human exploration of the oceans. However, research on underwater robots is still at the semiautonomous stage. Most of their underwater operations cannot be carried out without human participation. The main reason is that the complex underwater environment restricts the perception of robots. 3-D vision, as an important component of robot perception technology, has been widely used in obstacle avoidance [4], target grasping [5], simultaneous localization and mapping (SLAM) [6], and so on, which greatly improve the intelligence of robots. However, due to the special characteristics of the underwater environment (light absorption and particle scattering), common 3-D measurement devices, such as LiDAR and RGB-D cameras, cannot be used directly in the water. In addition, the acoustic-based underwater measurement technique has a long measurement distance but low accuracy and high noise level. For now, underwater high-precision 3-D reconstruction mainly relies on vision methods, which are divided into passive vision and active vision.

Passive vision [7] refers to the direct reception of light reflected from objects to acquire information, such as underwater cameras. Due to the poor quality of underwater imaging, image enhancement and recovery are generally required, which is technically difficult. In addition, underwater environments have fewer texture features compared to land, so current underwater 3-D reconstruction by passive vision can only be performed well in bright laboratory pools, which is hard to apply to underwater low-light environments.

In contrast to passive vision, active vision involves actively projecting specific light onto a target object and receiving its reflected light to achieve measurements. It is obvious that active vision can create artificial features that are more favorable to be extracted in the low-light underwater environment, so binocular stereo matching is easily achieved. In addition, laser rays contain enormous amounts of energy. It can be largely unaffected by particles in the water. For this reason, a binocular structured light vision measurement system is developed in this article to accomplish 3-D reconstruction in the low-light underwater environment.

The rest of this article is organized as follows. In Section II, the related work is outlined. Section III presents an overview of the developed system. Then, in Section IV, three models of

underwater refraction are proposed. A laser-based calibration algorithm is given in Section V, and the multiple experiments are conducted in Section VI. Finally, the conclusion and future work are provided in Section VII.

II. RELATED WORKS

As the need for underwater 3-D sensing is imminent, relevant underwater measurement devices based on different measurement principles have been developed, such as sonar, camera, and laser scanners.

A. Sonar

The first one is sonar [8], which utilizes the propagation and reflection characteristics of sound waves in the water to achieve ranging and navigation through electroacoustic conversion and information processing. To reconstruct an underwater cave, Mallios et al. [9] designed an AUV equipped with two mechanical imaging sonar sensors. The distance measurements in the horizontal and vertical directions of the robot were achieved, respectively. However, the reconstructed map motion distortion is severe due to the slow scanning speed of the mechanical sonar. In addition, the sonar has the problem of elevation angle ambiguity. Each pixel in the sonar image corresponds to a distance in a certain bearing range. No specific elevation angle information exists in the image, so it is not possible to determine the exact orientation of that distance [10]. Using a pair of wide-aperture imaging sonars with orthogonal uncertainty axes, McConnell et al. [11] independently observed the same point in the environment from two different perspectives. Then, dense and fully defined point clouds were created at each time step. However, this method is not suitable for general 3-D scenes due to the strong assumptions on object geometry. At present, 3-D image sonar is widely studied as the main sensor for underwater acoustic reconstruction [12]. Using an imaging sonar sensor, Westman et al. [13] presented a novel method for reconstructing particular 3-D surface points, which does not rely on the precise image intensity values or the reflectivity of the imaged surface to solve for the surface point locations according to Fermat flow equation. Then, a novel framework for object-level 3-D underwater reconstruction using imaging sonar sensors was presented by them [14]. In this framework, reconstruction reduces to a convex linear optimization problem with a variety of priors and regularization terms. Then, the alternating direction method of multipliers (ADMM) algorithm was used to solve it. Although both simulation and real data illustrate its superior reconstruction, the 3-D point cloud obtained using this approach is very sparse and not suitable for dense reconstruction.

B. Camera

Since sonar is only suitable for coarse measurements, while cameras have been very successful in accurate 3-D reconstruction in air, some underwater camera reconstruction methods have been proposed. First, some used monocular for reconstruction [15], [16]. Xiong and Heidrich [17] proposed a differentiable framework to estimate the geometry of underwater scenes and the time-varying water surface using ray casting, Snell's law, and multiview triangulation. However, the reconstruction framework relies on a preprocessed dense and precise correspondence matching. When the waves are driven by excessively strong external forces and become choppy, they are no longer in accord with the imposed smoothness regularizer, and the reconstruction quality degrades. In addition, the binocular stereo vision has been applied to underwater reconstruction [18], [19]. Among them, a novel approach was developed by Skinner et al. [20] in order to reduce the absorption of light by water. The estimation of the attenuation coefficient was integrated directly into the bundle adjustment step during the structure recovery of the underwater scene. This enables simultaneous estimation of the attenuation coefficients for nonlinear optimization. However, image recovery provides a limited improvement in image quality. In order to eliminate the effect of refraction in water, Berman et al. [21] made all of the images taken using a pair of DSLR cameras (Nikon D810 with an AF-S NIKKOR 35-mm f/1.8G ED lens, encased in a Hugyfot housing with a dome port) on a rigid rig. This must make the camera's optical center coincide with the sphere center of the circular cover, which is difficult to achieve, and inevitable error exists. Moreover, Kong et al. [22] proposed a refractive camera model and an akin triangulation by combining the underwater imaging laws. A nonlinear relationship between the object and its corresponding image plane points with the shell parameters was established. Then, an NSGA-II-Based Calibration Algorithm was developed to achieve the accurate calibration of the system. However, this method relies on the accurate extraction of the underwater checkerboard grid corner points. It cannot be applied to the underwater low-light environment.

C. Laser Scanner

It is obvious that passive vision represented by cameras is difficult to apply in most underwater environments, while active vision measurement methods based on laser scanning make their reconstruction possible [23], [24]. Currently, laser scanning can be divided into three types according to the form of scanning. The first type is not capable of scanning itself and relies on other systems. Wang et al. [25] proposed an underwater structured light vision calibration method considering an unknown refractive index and designed a prototype. It was loaded on a three-axis gantry to achieve underwater scene reconstruction. It is obvious that the reconstructed range of this scanning method is too dependent on the external platform motion, and less information is obtained from a single measurement. The second type is driven by an external motor, and the platform moves as a whole to achieve scanning. Based on this principle, Gu et al. [26] designed a laser-based scanner using a stepper motor to drive a laser and camera rotation. Then, a unified laser-based 3-D reconstruction method was proposed to realize high-accuracy measurement in various media, such as air, glass, and water. However, the presence of water resistance affects the scanning speed. The overall

movement of the platform also generates huge inertia, which is not suitable for the stability of the robot. The third type uses a mirror galvanometer to reflect a laser beam to achieve scanning. This is a static scanning method that does not affect the platform. Chi et al. [27] achieved underwater close-range 3-D reconstruction with high accuracy and resolution using a camera and a laser that is automatically scanned by a mirror galvanometer. Regardless of the scanning type, the above systems assume that the laser beams form a plane at the same moment. However, Palomer et al. [28] demonstrated that the laser plane of this structure is distorted when passing through different media (air-viewport-water). Then, he proposed two triangulation methods (ray-based and elliptical cone) [28]. The latter is more accurate, but more computationally complex. Castilln et al. [29] presented a novel 3-D laser scanner, which uses a two-axis mirror to project straight lines into the water by compensating for refraction-related distortions. Thus, plane models can be used without loss of accuracy, which is faster than the elliptic cones model. However, there are practical limitations to its system. The presented approach remains mainly at the level of theoretical research.

Although the above monocular laser scanning device has been able to perform underwater reconstruction tasks, there are some drawbacks. On the one hand, its hardware requirements are high as it needs to know the precise rotation angle of the mirror galvanometer in real time. On the other hand, its calibration process depends on the accurate modeling of the laser scanning surface, which Palomer proved to be nonplanar, so the modeling is complicated and the calibration is difficult. While the binocular ranging process is relatively simple, we hope to combine binocular and laser scanning for active underwater measurements. To the best of our knowledge, this article presents the first systematic complete modeling and laser-based calibration process of underwater 3-D reconstruction based on binocular structured light scanning.

It is worth mentioning that most of the abovementioned camera or laser scanner-based 3-D reconstruction systems are calibrated by extracting the corner point information of the checkerboard grid in different positions underwater [30]. However, for real underwater environments, passive vision-based corner point extraction can be very difficult in low-light conditions, resulting in large calibration errors or even calibration failure of the system parameters, so we would like to develop an active vision-based calibration method based on the geometric properties of the laser.

We summarize the contributions of our work as follows.

1) An underwater binocular structured light 3-D reconstruction system with the scanning laser is designed to realize the static high-precision scanning reconstruction of the low-light scene, which is suitable for underwater robot application, including grasping, surveying, and mapping. The obtained high-precision 3-D point clouds prove the effectiveness of our system.

2) Three models based on underwater refraction effects are systematically proposed, among which the multimedia binocular polar curve constraint model ensures accurate
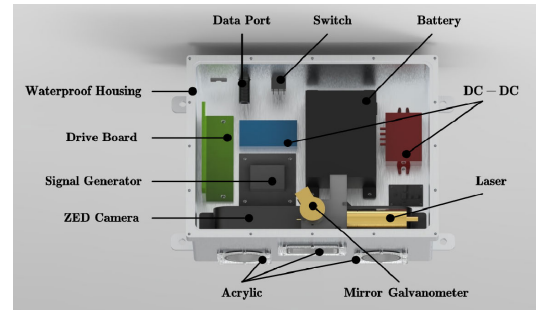

Fig. 1. Our underwater binocular structured light 3-D reconstruction system.

laser line matching, which is a relatively cutting-edge work.

3) A simple special calibration block is designed, and a new multiobjective laser-based calibration algorithm based on laser geometric constraints is proposed. The proposed method only needs one scanning data, which greatly simplifies the calibration process. More importantly, this method could achieve accurate calibration in the low-light underwater environment, which is hard for the checkerboard-based calibration method.

III. OVERVIEW OF SYSTEM

A. System Design

In order to improve the 3-D perception capability of underwater robots for better underwater operations, an active vision measurement system based on binocular structured light is designed (204 mm × 164 mm × 102 mm) in this article, and the further integration of this system into underwater robots is expected. The description of this underwater measurement system is illustrated in Fig. 1. The system consists of a binocular camera, laser, mirror galvanometer, power supply system, and waterproof housing, and the detailed hardware parameters are shown in Table I. Among them, the binocular camera selects the ZED camera. The laser type is MDL-SL∼520-30-CA13334, with a fan angle of 45°. The green laser was chosen because the water body absorbs less blue-green light than other light. The type of mirror galvanometer is s-8107. Its rotation speed and rotation status can be adjusted by the input signal. In this experiment, to mitigate the excessive transition state current, we set the input signal as a sine wave, which is provided by the signal generator ICL8038. In addition, the material of the light hole is acrylic, chemically known as polymeric methyl methacrylate (PMMA) with good light transmission and hardness. The power supply system is shown in Fig. 2. With the above design, our system can achieve object reconstruction within ±20° angle in the horizontal direction and ±22.5° angle in the vertical direction (about 400 sampling points per scan). Specifically, when the measurement distance is 0.5 m, the measurement range is about 0.41*0.36 m@0.5 m, and the laser resolution is about 1.025 mm@0.5 m.

B. System Principle

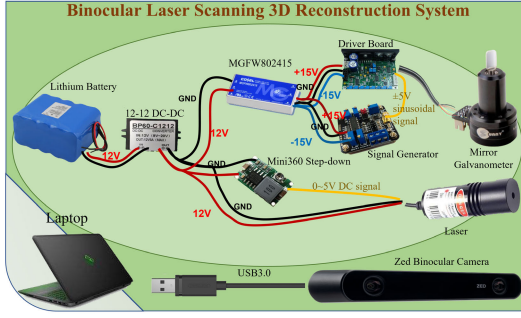Based on the previous hardware devices, our system can work in a low-light underwater environment. First, the internal

Fig. 2. Circuit design of our system.

TABLE I
SYSTEM HARDWARE PARAMETER TABLE

Hardware	Parameter	
ZED Camera	resolution	1280×720
	fps	60
Laser	wavelength	520nm
	power	30mW
ICL8038	amplitude	5V
	frequency	100mHz
BP60-C1212	input	920V
	output	12V
MGFW802415	input	$9 \sim 36V$
	output	$\pm 15V$
Mini360 Step-down	input	$4.75 \sim 23V$
	output	$1 \sim 17V$
Lithium Battery	voltage	12V
	capacity	6000mAh
Mirror-galvanometer	scanning angle	$\pm 20°$

and external parameters of the system (see Section V) are obtained by the calibration method, and the parameters are input to the measurement model (see Section IV). Then, the laser center is extracted and matched to obtain a series of matching points as input to the measurement model. The depth information corresponding to the laser lines is obtained by solving to obtain the point cloud data. Then, using laser scanning, the dense 3-D information of the scene is obtained, and the point cloud is processed using Point Cloud Library (PCL) to get the final 3-D reconstruction results (see Section VI).

1) Laser Center Extraction: Due to the dim underwater light and relatively simple scene elements, it is very unfavorable for binocular matching, but this characteristic is exactly beneficial for laser center extraction. First, the Gaussian filter is used to preprocess the image, and then, the gray centroid method is used to achieve subpixel extraction of the central profile of the laser stripe

$$U_m = \frac{\sum_{i=0}^{M} g_i \times u_i}{\sum_{i=0}^{M} g_i} \tag{1}$$

where U_m is the laser center pixel coordinate, u_i is the pixel coordinate of each point, and g_i is the gray value at that coordinate.

2) Laser Match: In order to achieve 3-D ranging, it is necessary to know the corresponding matching points of the left and right cameras, i.e., the position of a laser point in the left camera corresponding to the position in the right camera. For laser lines, it is difficult to determine the exact
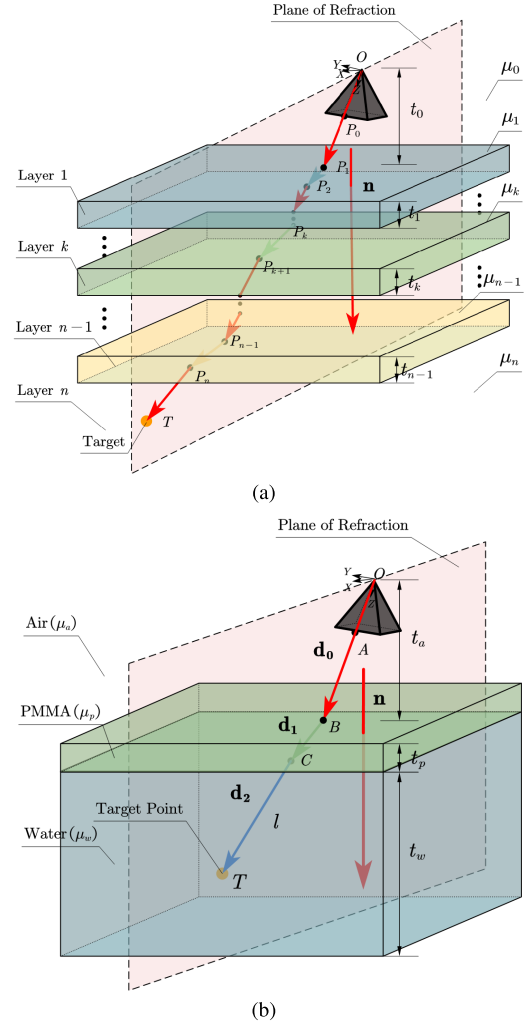

Fig. 3. Monocular ray-based refraction model. (a) Flat refractive geometry with n layers. (b) Monocular model of our system. Notations: the direction vectors of optical paths **OAB**, **BC**, and **CT** are $\mathbf{d_0}$, $\mathbf{d_1}$, and $\mathbf{d_2}$, respectively. t_a is the distance from the camera to the PMMA surface. t_p and t_w are the thickness of PMMA and water, respectively.

corresponding points in the left and right camera imaging planes due to the single feature. However, this can be easily achieved by our proposed polar curve constraint equation (see Section IV-C).

IV. SYSTEM MODEL

For terrestrial environments, the monocular pinhole imaging model and the binocular triangulation model play an important role in 3-D reconstruction. The proposed polar line constraint model, on the other hand, significantly improves the accuracy of binocular matching. However, the above three models are no longer work underwater. In order to perform underwater measurements, this article presents a relevant study on the underwater camera model, which provides a rigorous theoretical basis for systematic measurements.

A. Monocular Ray-Based Refraction Model

During the imaging process of our camera, light in this system passes through Water-PMMA and PMMA-Air and,

finally, converges to the camera imaging plane. Because of the refraction effect, the traditional pinhole imaging model will no longer be applicable to this system camera. Therefore, the camera imaging process under the multilayer refraction plane is studied. As shown in Fig. 3(a), it is assumed that there are multiple layers of media with different refractive indices (Layer k, $k = 1, \ldots, n$) between the target point T and the camera optical center O. The intersection points of light and each medium are $\{P_1, P_2, \ldots, P_n\}$, and the intersection point of the optical path with the imaging plane is P_0. The camera coordinate system $\{W\}$ is used as the base coordinate system, and each medium plane is parallel to each other. The normal vectors are all $\mathbf{n}$. According to the principle of the refraction plane proposed by Agrawal et al. [31], $\mathbf{P_0 P_1}, \mathbf{P_1 P_2}, \ldots, \mathbf{P_k P_{k+1}}, \ldots, \mathbf{P_n P}$ are coplanar, all on the refraction plane Π. There are

$$\mathbf{P_{i+1} P_{i+2}} = \alpha_{i+1} \mathbf{P_i P_{i+1}} + \beta_{i+1} \mathbf{n} \tag{2}$$

where α_{i+1} and β_{i+1} are arbitrary real numbers, $i = 0, \ldots, n$.

For our system, there are only three media: air, PMMA, and water, with refractive indices of μ_a, μ_p, μ_w, and $\mu_a < \mu_w < \mu_p$, as shown in Fig. 3(b). For the direction vector $\mathbf{d_0}$, there is

$$\mathbf{d_0} = \frac{\mathbf{AB}}{|\mathbf{AB}|} = \frac{\mathbf{OA}}{|\mathbf{OA}|}. \tag{3}$$

When the image point p of the target point on the imaging plane of the camera is known, the coordinates of P_0 can be easily found using the internal reference formula of the camera

$$\begin{bmatrix} p \\ 1 \end{bmatrix} = K P. \tag{4}$$

Because the distance of the camera optical center from the refractive plane is t_a, the coordinate point of P_1 is

$$B = \frac{t_a}{\mathbf{d_0} \cdot \mathbf{n}} \mathbf{d_0}. \tag{5}$$

Furthermore, according to (2), it is obtained that

$$\mathbf{d_1} = \alpha_1 \mathbf{d_0} + \beta_1 \mathbf{n} \tag{6}$$
$$\mathbf{d_2} = \alpha_2 \mathbf{d_1} + \beta_2 \mathbf{n}. \tag{7}$$

Based on Snell's law, we can solve that

$$\begin{cases} \alpha_1 = \dfrac{\mu_a}{\mu_p} \\ \alpha_2 = \dfrac{\mu_p}{\mu_w} \\ \beta_1 = \sqrt{1 - \alpha_1^2[1 - (\mathbf{d_0} \cdot \mathbf{n})^2]} - \alpha_1 \mathbf{d_0} \cdot \mathbf{n} \\ \beta_2 = \sqrt{1 - \alpha_2^2[1 - (\mathbf{d_1} \cdot \mathbf{n})^2]} - \alpha_2 \mathbf{d_1} \cdot \mathbf{n} \end{cases}$$

also for

$$\mathbf{BC} = \frac{t_p}{\mathbf{d_1} \cdot \mathbf{n}} \mathbf{d_1}. \tag{8}$$

Thus,

$$C = B + \frac{t_p}{\mathbf{d_1} \cdot \mathbf{n}} \mathbf{d_1} = \frac{t_a}{\mathbf{d_0} \cdot \mathbf{n}} \mathbf{d_0} + \frac{t_p}{\mathbf{d_1} \cdot \mathbf{n}} \mathbf{d_1}. \tag{9}$$
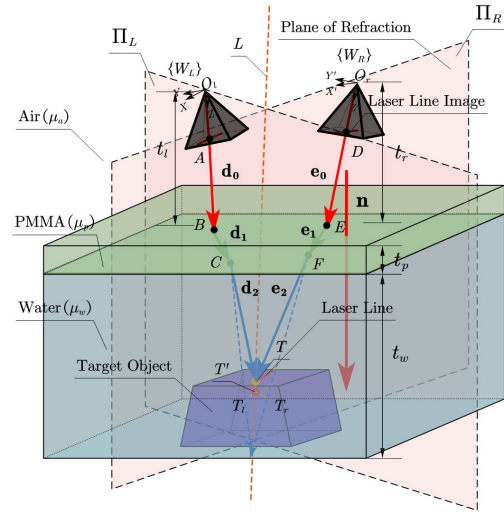

Fig. 4. Binocular triangulation-like refraction model. Notations: $\mathbf{d_0}$, $\mathbf{d_1}$, and $\mathbf{d_2}$ are the direction vectors of the optical path $\mathbf{O_l AB}$, $\mathbf{BC}$, and $\mathbf{CT_l}$ of the left camera. $\mathbf{e_0}$, $\mathbf{e_1}$, and $\mathbf{e_2}$ are the direction vectors of the optical path $\mathbf{O_r DE}$, $\mathbf{EF}$, and $\mathbf{FT_r}$ of the right camera. Solid lines $\mathbf{CT}$ and $\mathbf{FT}$ are ideal optical paths, and dotted lines $\mathbf{CT_l}$ and $\mathbf{FT_r}$ are actual optical paths. t_l and t_r are the distances from the left camera and the right camera to the PMMA surface, respectively.

Combining (3)–(9), we can calculate the coordinate points of C and $\mathbf{d_2}$. So far, the equation of the line $l : CT$ can be obtained

$$l : \quad T = C + m\mathbf{d_2}, \quad m > 0 \tag{10}$$

where m is a free variable. Because of it, a single camera cannot determine the specific location of the target point T.

B. Binocular Triangulation-Like Refraction Model

It is obvious that just a single camera has no scale information to obtain the specific location of the target point. Using two cameras, a point can be uniquely determined by two optical paths to achieve depth measurement, as shown in the specific model of Fig. 4.

From the previous analysis in Section IV-A, C^1, F^2, $\mathbf{d_2^1}$, and $\mathbf{e_2^2}$ can be easily obtained. We agree that 1 in the upper right corner of all the letters means under the coordinate system $\{W_L\}$ and 2 means under $\{W_R\}$. Satisfy the following conversion relationship:

$$X^1 = R X^2 + T \tag{11}$$

where X represents any coordinate, and R and T are the calibrated rotation and translation matrices, respectively. Thus, F^1 and $\mathbf{e_1^1}$ by F^2 and $\mathbf{e_2^2}$ can be known.

In addition, t_l and t_r are also related as follows:

$$t_r = t_l - T \cdot \mathbf{n^1}. \tag{12}$$

From above, the line $l_L : CT$ and the line $l_R : FT$ can be calculated, and the intersection point of the two is the coordinates of the requested target point. That is,

$$\begin{cases} T = C^1 + m_L \mathbf{d_2^1} \\ T = F^1 + m_R \mathbf{e_2^1} \end{cases} \tag{13}$$
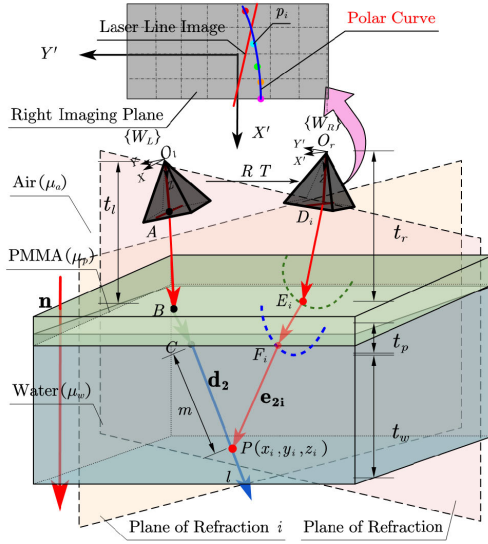
Fig. 5. Underwater polar curve constraint model. Notations: P is a possible target point, corresponding to different optical paths $\mathbf{O_r D_i F_i P}$ and p_i on the imaging plane of the right camera. The direction vector of $\mathbf{F_i P}$ is $\mathbf{e_{2i}}$.

where m_L and m_R are free variables and can be eliminated to obtain the coordinates of T.

However, in the actual process, the straight lines l_L and l_R may be heterogeneous due to the existence of systematic errors, i.e., $(\mathbf{C^1 F^1} \times \mathbf{d_2^1}) \cdot \mathbf{e_2^1} \neq 0$, as shown by the dotted line $\mathbf{CT_l}$ and $\mathbf{FT_r}$ in Fig. 4.

The equations of the left plane of refractive Π_L and the right plane of refractive Π_R can be easily derived from the geometric point relations as follows:

$$\Pi_L : \quad \left(P_l - A^1, \mathbf{d_0^1}, \mathbf{n^1}\right) = 0$$
$$\Pi_R : \quad \left(P_r - D^1, \mathbf{e_0^1}, \mathbf{n^1}\right) = 0 \tag{14}$$

where P_l, P_r is any point on the plane Π_L, Π_R.

Therefore, the equation of the line of intersection L of the two planes can be found

$$L : \quad \begin{cases} \left(T' - A^1, \mathbf{d_0^1}, \mathbf{n^1}\right) = 0 \\ \left(T' - D^1, \mathbf{e_0^1}, \mathbf{n^1}\right) = 0 \end{cases} \tag{15}$$

where T' is any point on the line L.

It can be known that the imaginary point of the two optical paths must be on the straight line L, so the target point we consider must be on L. For this reason, the target point is defined as a point on L with the minimum sum of the distance from l_L and l_R. That is,

$$T = \arg \min_{T} \left(\left| \mathbf{TC^1} \times \mathbf{d_2^1} \right| + \left| \mathbf{TF^1} \times \mathbf{e_2^1} \right| \right)$$
$$\text{s.t.} \begin{cases} \left(T - A^1, \mathbf{d_0^1}, \mathbf{n^1}\right) = 0 \\ \left(T - D^1, \mathbf{e_0^1}, \mathbf{n^1}\right) = 0. \end{cases} \tag{16}$$

C. Underwater Polar Curve Constraint Model

In binocular stereo matching, polar line constraint is an important property that can be used to achieve polar line correction for faster and more accurate matching results. However, due to the existence of multiple media, the underwater

binocular camera no longer satisfies the polar line constraint, but we find that the matching points of the left and right cameras still have a similar constraint, which we call the polar curve constraint here, as shown in Fig. 5. Assuming that a point p_L is known under the left camera image coordinate system, the purpose of the polar curve constraint is to find the possible location of p_L in the right camera image coordinate system.

By using the monocular ray-based refraction model in Section IV-A, the expression of the line l can be deduced with the known p_L

$$l : \quad P = C^1 + m\mathbf{d_2^1}, \quad m > 0 \tag{17}$$

where P is any point on the line l. m is the linear parameter variable, and its value indicates the distance from point P to point C. Apart from that, all other parameters can be solved by known p_L by (2)–(9).

Thus, there is a mapping between the coordinates of the point P in $\{W_L\}$ coordinate system and the variable m, which can be abbreviated as

$$P^1 = f(m, p_L). \tag{18}$$

Suppose that the coordinate of P under the right camera coordinate system $\{W_R\}$ is P^2, using

$$P^1 = R P^2 + T. \tag{19}$$

The coordinates of P^2 can also be denoted by m

$$P^2 = R^T (f(m, p_L) - T) = g(m, p_L). \tag{20}$$

Suppose that the coordinates of point P are (x^2, y^2, z^2); then, x, y, and z can also be abbreviated as

$$\begin{cases} x = g_x(m, p_L) \\ y = g_y(m, p_L) \\ z = g_z(m, p_L). \end{cases} \tag{21}$$

Similarly, assume that there is a point p_i in the right camera image coordinate system. The coordinates of F_i^2 and the direction vector of the line $\mathbf{e_i^2}$ can be expressed in terms of p_i in the $\{W_R\}$ coordinate system, which may be set as $(F_x(p_i), F_y(p_i), F_z(p_i))$ and $(e_x(p_i), e_y(p_i), e_z(p_i))$. Then, the line $F_i^2 P^2$ can be expressed using the coordinates of p_i

$$\frac{X - F_x(p_i)}{e_x(p_i)} = \frac{Y - F_y(p_i)}{e_y(p_i)} = \frac{Z - F_z(p_i)}{e_z(p_i)}. \tag{22}$$

$P^2(x^2, y^2, z^2)$ can be known from (21). Plug it into (22)

$$\begin{cases} (g_x(m, p_L) - F_x(p_i))e_y(p_i) = (g_y(m, p_L) - F_y(p_i))e_x(p_i) \\ (g_y(m, p_L) - F_y(p_i))e_z(p_i) = (g_z(m, p_L) - F_z(p_i))e_y(p_i). \end{cases} \tag{23}$$

The above equation is the polar curve constraint equation satisfied by the point p_i under the right camera image coordinate system corresponding to the point p_L under the left camera image coordinate system. It can be known that this curve is only related to the variable m.

V. LASER-BASED CALIBRATION METHOD

According to the model analysis in Section IV, the whole system parameters include the following.

1) *Camera Internal Parameters:* $\{K_L, K_R\}$.
2) *Camera External Parameters:* $\{R, T\}$.
3) *House Parameters:* $\{\mathbf{n}, t_l, t_r, t_p, \mu_a, \mu_p, \mu_w\}$.

Among them, the calibration of the internal and external parameters of the camera can be performed in the air. This type of parameter calibration method has been relatively mature. The method represented by Zhang's [32] calibration method has been able to solve this kind of problem quite well. Therefore, the air calibration part of this article is implemented by the MATLAB calibration toolbox and will not be discussed further. For the House Parameter part, $\{\mu_a\}$ is a constant and can be easily obtained by searching the data, while $\{t_l, t_r, t_p\}$ can only be roughly measured by physical means and needs to be further calibrated. $\{t_l, t_r\}$ has a constraint relation [see (12)], and only one of them needs to be calibrated. Moreover, $\{\mathbf{n}\}$ is a unit vector with intrinsic geometric constraints, so only $\{\mathbf{n}_x, \mathbf{n}_y\}$ needs to be calibrated. Considering that our measurement system is mainly used for underwater reconstruction in different environments, the refractive index of water is changed by the influence of dissolved substances in the water. Therefore, the refractive index of water cannot be considered a constant. It needs to be calibrated underwater. Different manufacturers produce PMMA with different refractive indices, which also need to be calibrated. In summary, the housing parameters that need to be calibrated underwater in our system include $\{t_l, t_p, \mathbf{n}_x, \mathbf{n}_y, \mu_w, \mu_p\}$. Namely,

$$P = f(t_l, t_p, \mathbf{n}_x, \mathbf{n}_y, \mu_w, \mu_p). \tag{24}$$

A. Design of Calibration Block

In order to achieve the calibration of unknown parameters, some 2-D–3-D matching points are usually needed for system parameter identification. However, for a real underwater environment, the exact 3-D point coordinates are difficult to obtain. In this system, the laser beam falling on a plane creates a natural colinear geometric constraint, so a multiobjective optimization is adopted to achieve the parameter calibration. The scale problem cannot be solved by using only the laser line geometry constraint, so a simple specific calibration block is designed to realize the calibration. As shown in Fig. 6, the calibration block consists of two parts: calibration plane and alignment line. Among them, the calibration plane is 200 mm × 100 mm. The alignment line is perpendicular to the calibration block and serves as the initial scanning reference for the laser line. The background is arbitrary, and the physically calibrated underwater environment can be considered as it.

B. Laser-Based Calibration Method-Based Optimization

During the calibration process, adjust the position of the calibration block so that the laser line is aligned with the alignment line on the calibration block (deviations are allowed here and have no effect on the calibration algorithm). Then, fix the calibration block and the measuring device, and turn
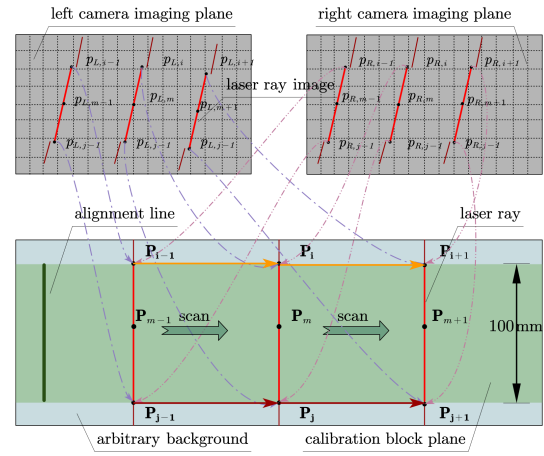

Fig. 6. Laser-based calibration method-based optimization.

on the laser for scanning. As shown in Fig. 6, when the laser is scanned, a point pair $\{(P_i, P_j)|i = j = 1, 2, \ldots, N\}$ is generated at the edge of the calibration plane, and each midpoint is noted as a pair $\{P_m|m = 1, 2, \ldots, N\}$, which correspond to the left camera imaging plane $\{(p_{L,i}, p_{L,j}, p_{L,m})|i = j = m = 1, 2, \ldots, N\}$ and the right camera imaging plane $\{(p_{R,i}, p_{R,j}, p_{R,m})|i = j = k = 1, 2, \ldots, N\}$, respectively. It is obvious that $\{(p_{L,k}, p_{R,k})|k = i, j, m = 1, 2, \ldots, N\}$ is a strict matching point relationship, which is substituted into the measurement model in Section III to obtain $\{(P_i, P_j, P_m)|i = j = m = 1, 2, \ldots, N\}$, the 3-D coordinates of each point. Of course, these coordinates cannot be derived specifically at this time and contain parameters to be calibrated. Namely,

$$P_n = f(t_l, t_p, \mathbf{n}_x, \mathbf{n}_y, \mu_w, \mu_p, p_{L,k}, p_{R,k})$$
$$k = i, j, m = 1, 2, \ldots, N. \tag{25}$$

However, $\{(P_i, P_j, P_m)|i = j = m = 1, 2, \ldots, N\}$ points satisfy the following constraint relations.

1) *Scale Constraint:* The lengths of $\min_{j=1}^{N} |\mathbf{P_i P_j}|$ are the width w of the calibration plane

$$\text{loss}_1 = \sum_i^N \left| \min_{j=1}^N \left| \mathbf{P_i P_j} \right| - w \right|. \tag{26}$$

2) *Isometric Constraint:* $P_{i-1}P_i$ is equal in length to $P_{j-1}P_j$

$$\text{loss}_2 = \sum_{i=j=1}^N ||\mathbf{P_{i-1}P_i}| - |\mathbf{P_{j-1}P_j}||. \tag{27}$$

3) *Parallel Constraint:* $P_{i-1}P_i$ is parallel to $P_{j-1}P_j$

$$\text{loss}_3 = \sum_{i=j=1}^N \left| \frac{\mathbf{P_{i-1}P_i} \cdot \mathbf{P_{j-1}P_j}}{|\mathbf{P_{i-1}P_i}||\mathbf{P_{j-1}P_j}|} - 1 \right|. \tag{28}$$

4) *Colinear Constraint:* P_m on $P_i P_j$

$$\text{loss}_4 = \sum_{i=j=m=1}^N \left(\sqrt{|\mathbf{P_i P_j}|^2 - \frac{(\mathbf{P_i P_m} \cdot \mathbf{P_i P_j})^2}{|\mathbf{P_i P_m}|^2}} \right). \tag{29}$$

Algorithm 1 Calibration Algorithm

Input: x: house parameters initial value

  i: number of interactions;

  ω: inertia weight; c_1, c_2: learning factors;

  (w_1, w_2, w_3, w_4): loss weights

Output: optimal $t_l, t_p, \mathbf{n}_x, \mathbf{n}_y, \mu_w, \mu_p$

1: Random initialization of population parameters: x_0, v_0
2: Laser centerline extraction, see Eq. (10) for details
3: Laser point extraction at the edge of the calibration plate:
  $set\{(p_l, p_r)\}$
4: **for** $j = 0$ to i **do**
5:   get 3-D coordinates from our binocular refraction model
  (Section IV-B): $P = model(p_l, p_r, m)$
6:   calculate scale constraint loss: l_1 (Eq. (26))
7:   calculate isometric constraint loss: l_2 (Eq. (27))
8:   calculate parallel constraint loss: l_3 (Eq. (28))
9:   calculate co-linear constraint loss: l_4 (Eq. (29))
10:   get all loss: l (Eq. (30)), calculate fitness: $f = 1/l$
11:   **if** $f >= \varepsilon$ (minimum expectation) **then**
12:     break
13:   **end if**
14:   update individual optimum $pbest_j$ and population optimum $gbest_j$
15:   update velocity:
  $v_j = v_j + c_1 \times (pbest_j - x_j) + c_2 \times (gbest_j - x_j)$
16:   update position:
  $x_j = x_j + v_j$
17:   $j = j + 1$
18: **end for**

Combining the above constraints

$$\text{loss} = w_1 \text{loss}_1 + w_2 \text{loss}_2 + w_3 \text{loss}_3 + w_4 \text{loss}_4 \quad (30)$$

where $w_1, w_2, w_3, w_4 > 0$ are weight parameters.

For the calibration task, it is sufficient to optimize the parameters to be calibrated in such a way that the loss is minimized

$$t_l, t_p, \mathbf{n}_x, \mathbf{n}_y, \mu_w, \mu_p = \underset{t_l, t_p, \mathbf{n}_x, \mathbf{n}_y, \mu_w, \mu_p}{\arg\min} \text{loss}. \quad (31)$$

In addition, the initial values of t_l and t_p can be obtained by physical measurements. Since the binocular camera is basically parallel to the PMMA surface, the initial values of $\mathbf{n}_x$ and $\mathbf{n}_y$ only need to be chosen at any value around 0, such as -0.2. The initial value of μ_w can be taken as the refractive index of pure water 1.33. By consulting the datasheet, the refractive index of PMMA is in the interval [1.4, 1.6], so the initial value can be set to 1.4. At this point, the system calibration task is transformed into a multiobjective optimization problem with known initial values. Evolutionary algorithms, such as particle swarm optimization, can be used to easily obtain the optimal set of parameters with known initial values, as shown in Algorithm 1.
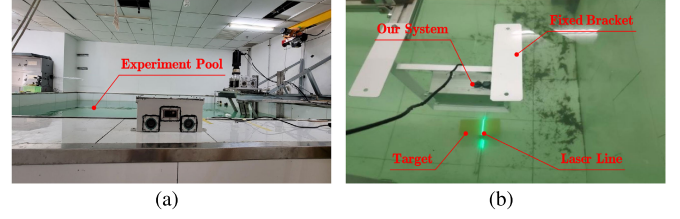

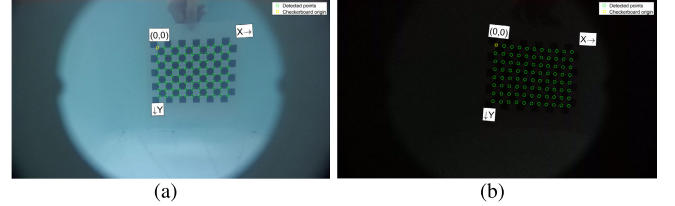Fig. 7. Illustration of our experiment scene and system. (a) Experiment pool. (b) Our system.

Fig. 8. Camera imaging results of underwater scenes with different light intensities. (a) Bright underwater scene. (b) Low-light underwater scene.

VI. EXPERIMENTS AND RESULTS

A. Experimental Setup

As shown in Fig. 7(a), experiments are carried out in a $5 \times 4 \times 1.5$ m pool. Fig. 7(b) shows that our binocular structured light system is scanning to reconstruct the target object. During the experiment, the system is fixed in the water by a metal bracket. Then, we control the mirror galvanometer so that the laser scans the target object at the bottom of the pool. The binocular camera captures the laser lines and obtains matching pixel point pairs by our pole curve constraint model. Then, the 3-D points of the target object can be obtained through the binocular triangulation-like refraction model proposed above.

B. Calibration Results

Currently, most underwater calibration experiments still rely on a checkerboard grid. Its key step is the extraction of corner points by image processing. The system can then be calibrated by the physical constraint relationships between the corner points. This approach is commonly used in the air environment. However, for the underwater low-light environment, the extraction of corner points is very difficult, which seriously affects the calibration accuracy. As shown in Fig. 8, the checkerboard grid can be detected accurately in bright underwater environments, while, for low-light conditions, the checkerboard grid cannot be detected accurately.

To measure the feasibility quantitatively, we use the MATLAB binocular camera calibration toolbox to obtain the corner point reprojection error of the checkerboard grid for both scenarios. As shown in Fig. 9, the reprojection error is about 0.25 pixels for the bright scene, which is acceptable. However, for the low-light condition, the reprojection error is about 0.65 pixels, which is more than 0.5 pixels, and the error is not tolerable. Moreover, we collect a total of 49 pairs of binocular images, and 21 pairs are rejected during the calibration. In conclusion, it is clear that the checkerboard grid-based calibration method is no longer applicable in low-light conditions.
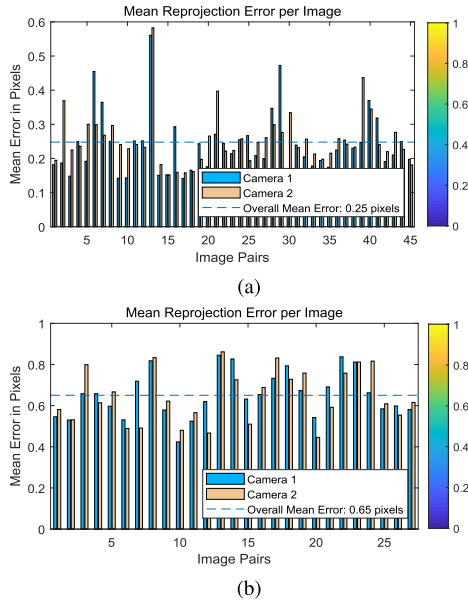
(a)

(b)

Fig. 9.   Reprojection errors of checkerboard grid corner points in different underwater environments. (a) Bright underwater scene. (b) Low-light underwater scene.

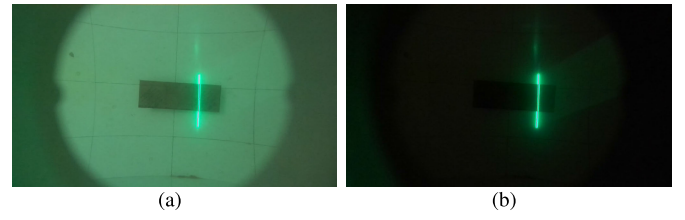(a)   (b)

Fig. 10.   Centerline extraction results of different light intensity (shown in red). (a) Bright underwater scene (18.3 lx). (b) Low-light underwater scene (0.8 lx).
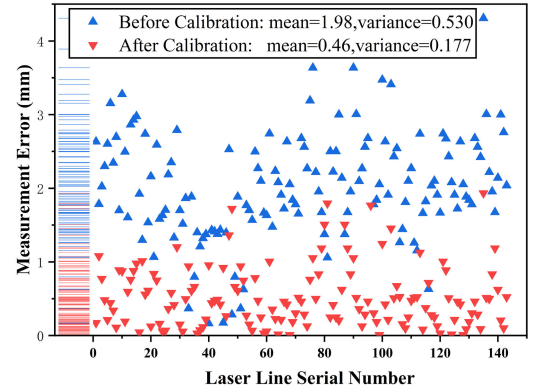

Fig. 11.   Comparison of measurement error before and after calibration.

(a)   (b)   (c)

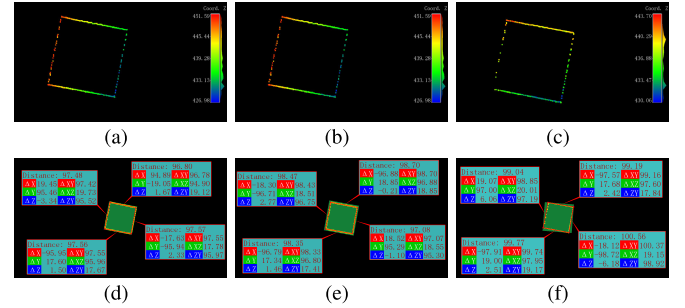(d)   (e)   (f)

Fig. 12.   Measurement results of underwater objects with a square surface (about 100 mm). (a) Edge point cloud obtained by triangulation model (air). (b) Measurement result by triangulation model (water). (c) Edge point cloud obtained by our proposed binocular triangulation-like refraction model. (d) Measurement result by triangulation model (air). (e) Edge point cloud obtained by triangulation model (water). (f) Measurement result by our proposed binocular triangulation-like refraction model.

In order to achieve high-accuracy calibration of the system in the low-light underwater environment, a simple calibration block with known width is designed, and the calibration task is transformed into a multiobjective optimization problem based on the geometric characteristics of the system laser. As shown in Fig. 10, centerline extraction works well, both in normal and low-light scenes. The proposed laser-based calibration algorithm only requires one scanning data, which greatly simplifies the calibration process. The specific algorithm is shown in algorithm 1. During the experiment, the initial parameters and the calibration results are shown in Table II. From the calibration results, the values of each parameter are close to the physical measurements, reflecting the reasonableness of our calibration method.

In the experiment, the width of the calibration block plane is chosen to be 99.94 mm, and the calibration data is obtained by one scan. As shown in Fig. 11, using the initial parameters before calibration, the average measurement error is 1.98 mm, and the average measurement width is 97.96 mm. After the proposed algorithm optimization, the average measurement error is 0.46 mm, and the average measurement width is 99.99 mm. Moreover, the error variances before and after calibration are 0.530 and 0.177, respectively. Therefore, our proposed calibration algorithm can significantly improve the measurement accuracy and stability of the system.

C. Measurement Results

Three sets of experiments are carried out to verify the robustness of the system measurement. The first set of experiments is to measure objects of different shapes and sizes, the second set is to measure objects of different materials, and the third set is to measure the same objects at different distances. In addition, to verify the superiority of our proposed binocular triangulation-like refraction model, comparative measurements are performed for each measurement.

1) Measurement Results of Different Shapes and Sizes: In order to obtain the measurement results of our system for objects of different shapes and sizes in the low-light underwater environment, we fix it at a height of about 500 mm from the bottom of the pool and measured the surfaces of different objects (plastic) at the bottom of the pool, including circle 1, circle 2, square 1, square 2, and equilateral triangle 1, similar to Fig. 10(b).

In the actual measurement process, we only need to use the pixel coordinates of the center of the laser line at the edge of the left and right camera imaging planes and substitute them into the imaging model to obtain the edge 3-D coordinates, as shown in Fig. 12.

TABLE II
SYSTEM CALIBRATION RESULTS

parameter name	t_l	t_p	$\mathbf{n}_x$	$\mathbf{n}_y$	μ_w	μ_p
initial value interval	[0,30]	[2,6]	[-0.2,0.2]	[-0.2,0.2]	[1.33,1.34]	[1.4,1.6]
initial parameter	30	2	-0.2	-0.2	1.33	1.4
optimization result	**26.7103**	**2.7310**	**-0.0991**	**-0.0371**	**1.3384**	**1.5092**

TABLE III
MEASUREMENT RESULTS OF DIFFERENT SHAPES, SIZES, AND MATERIALS

Material	Surface shape	True Size (mm)	Triangulation model (air) (mm)	Triangulation model (water) (mm)	Our Refraction Model (mm)
plastic	circle 1	59.84	62.31 (4.13%)	61.26 (2.37%)	**60.19 (0.58%)**
	square 1	69.93	67.83 (3.00%)	68.36 (2.25%)	**69.58 (0.50%)**
	circle 2	99.86	96.08 (3.79%)	100.78 (0.92%)	**99.33 (0.53%)**
	square 2	99.80	97.35 (2.45%)	98.15 (1.65%)	**99.64 (0.16%)**
	triangle 1	129.47	126.51 (2.29%)	127.73(1.34%)	**130.11 (0.49%)**
metal	circle3	59.92	61.87 (3.20%)	60.59 (1.11%)	**59.71 (0.35%)**
	square 3	70.00	67.83 (3.10%)	68.80 (1.71%)	**70.39 (0.56%)**
	circle 4	99.94	98.17 (1.77 %)	99.22 (0.72 %)	**100.57 (0.63%)**
	square 4	99.97	96.29 (3.68%)	96.90 (3.07%)	**99.29 (0.68%)**
	triangle 2	129.71	124.78 (3.80%)	126.79 (2.25%)	**128.58 (0.87%)**
wood	circle5	61.09	59.38 (2.80%)	59.95 (1.87%)	**60.79 (0.49%)**
	square 5	69.90	68.16 (2.49%)	68.51 (1.99%)	**69.47 (0.62%)**
	circle 6	99.85	96.67 (3.18%)	97.67 (2.18%)	**100.52 (0.67%)**
	square 6	100.01	95.97 (4.04%)	97.97 (2.04%)	**99.32 (0.69%)**
	triangle 3	129.29	126.87 (1.87%)	127.69 (1.24%)	**129.85 (0.43%)**

TABLE IV
RECONSTRUCTION RESULTS AT DIFFERENT TURBIDITIES

Turbidity	Shapes	Variance	Average Error	True Radius	Fit Radius
low	plane circle	0.71	0.47	-	-
	plane square	0.96	0.66	-	-
	cubic hemisphere	1.2	0.92	49.59	49.47
middle	plane circle	1.55	1.23	-	-
	plane square	1.78	1.59	-	-
	cubic hemisphere	1.72	1.48	49.59	50.15
high	plane circle	2.86	2.85	-	-
	plane square	2.54	2.01	-	-
	cubic hemisphere	2.41	2.02	49.59	48.25

In the same way, the dimensions of the surface of a variety of objects underwater are measured, as shown in Table III (plastic). By analyzing the errors, it is obvious that our proposed refraction model has the smallest measurement errors, and all of them are less than 1 mm. For all types of planes, the average measurement error is within 1%. There is no doubt that the triangular model calibrated in the air has the largest error (2%–4%). The model calibrated in water, on the other hand, aims to trim the effect of underwater refraction effects using aberration correction. The measurement error is reduced, in the range of 1%–2.5%, but it is still large, and the measurement accuracy is smaller than our refraction model. In conclusion, the underwater refraction effect cannot be treated simply as an aberration. The proposed refraction model can effectively reduce its impact.

2) Measurement Results of Different Materials: In order to verify the effectiveness of the system for measuring different materials, two additional sets of experiments were implemented on the basis of the abovementioned target objects made of plastic. In this case, the additional target objects were made of metal and wood, respectively. The results of all experiments are shown in Table III. From the experimental results, it can be seen that the measurement accuracy of plastic objects is slightly higher than metal and wood objects. This is due to the different reflections of different materials for laser light. The metal surface is too smooth and reflects strongly. The wood surface is too rough and has severe diffuse reflection. These factors will affect the extraction of the center line of the laser stripe, which will produce noise during the measurement process and affect the measurement accuracy. However, these noise points are few and do not affect the overall measurement results. In summary, the proposed binocular structured light vision measurement system can obtain satisfactory results for objects of different materials, which is applicable for most underwater measurement scenes.

3) Measurement Results at Different Distances: In order to obtain the measurement results of the system at different distances, the system is fixed at the heights of about 500, 700, and 900 mm from the bottom of the pool, respectively. As is shown in Fig. 13, the object with a side length of about 130-mm equilateral triangle on the surface of the pool bottom was scanned and measured, and its edge point cloud was obtained in the same way as above. The measurement error is shown in Fig. 14. It can be seen that the measurement error generally increases as the measurement distance increases, but our refraction model is also all much smaller than the triangulation model error. To the best of our knowledge, our system achieves state-of-the-art measurement accuracy for the same underwater measurement distance. This accuracy is more than sufficient for our future robotic operations.

D. Underwater 3-D Reconstruction Results at Different Turbidities

In order to further verify the performance of our system, 3-D measurement experiments of two regular planes, a hemi-

TABLE V

COMPARISON OF STATE-OF-THE-ART METHODS FOR UNDERWATER MEASUREMENT AND 3-D RECONSTRUCTION

| System	Kong's [22]	Anwer's [34]	Gu's [26], Xue's [35]	Detry's [36]	Our system
fundamental principle	stereo vision	time-of-flight	monocular structured light	binocular structured light	binocular structured light
measurement accuracy	>97.5%	>99.0%	>99.0%	——	>99.0%
measurement distance	<1m	0.35-0.65m	>1m	>1m	>1m
calibration requirement	checkboard-based	——	checkboard-based	checkboard-based	laser-based
	high-light	high-light	high-light	high-light	low-light
turbidity requirement	clear water	clear water	——	1-2.5 NTU	<30 NTU
system stability	stationary	stationary	huge inertia	stationary	stationary
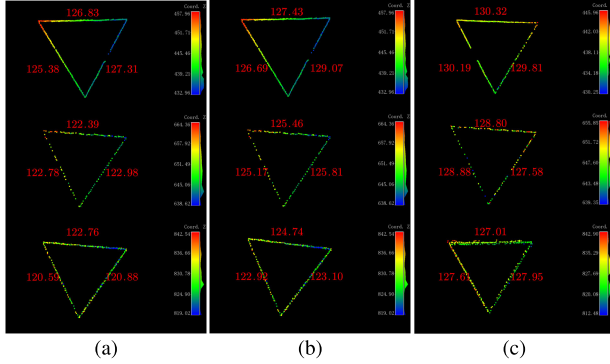
Fig. 13. Measurement results of triangle 1 at different distances. The first to the third row corresponds to about 500, 700, and 900 mm, respectively. (a) Measurement results by triangulation model (water). (b) Measurement results by triangulation model (water). (c) Measurement results by our proposed binocular triangulation-like refraction model.
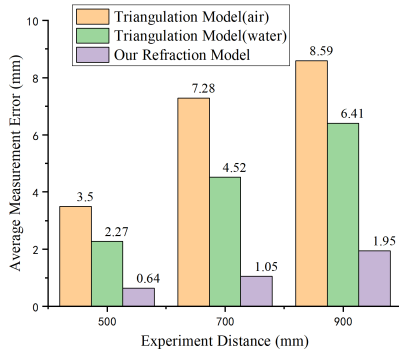

Fig. 14. Average measurement errors at different distances.
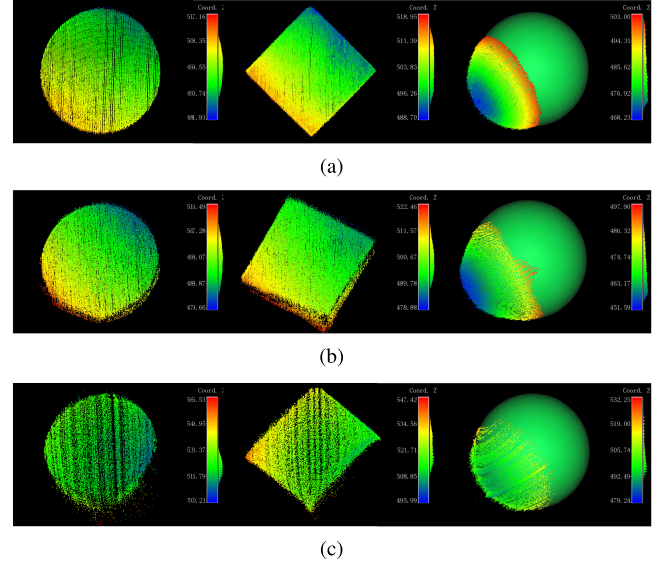

Fig. 15. Reconstruction results of regular shapes with different turbidity levels. (a) Low turbidity. (b) Middle turbidity. (c) High turbidity.

shown in Table IV. It can be seen that, in the low turbidity water environment, the average error of our system reconstruction is within 1 mm, which achieves high accuracy. With the increase in turbidity, the average error and variance become larger. The average reconstruction error of the system at high turbidity does not exceed 3 mm, and the fit sphere radius error does not exceed 2 mm. This is due to the increasing attenuation of the laser in the water as the turbidity increases, which makes the extraction of the laser center line more and more difficult. However, the underwater reconstruction result is satisfactory even for the complex underwater environment because measurement accuracy is sufficient for our future robotic manipulation.

2) Reconstruction Results for Irregular Shape (Starfish): To further verify the robustness of the system under different turbidity levels, an irregular starfish was reconstructed, as shown in Fig. 16(a). In order to quantitatively compare the reconstruction results, the 3-D point cloud ground truth of the starfish needs to be acquired, which is achieved in the experiment by a high-precision depth camera (Mech-Eye Nano) in air, as shown in Fig. 16(b). Fig. 16(c), (e), and (g) shows the starfish reconstruction results of our system under water with different turbidity levels, respectively. Then, the iterative closest point (ICP) matching algorithm is applied between the true value and the point cloud obtained by our system. The matching results are shown in Fig. 16(d), (f), and (h). The root mean square (rms) is 0.499, 1.164, and 1.579 for different

sphere, and an irregular starfish under a low-light underwater environment have been carried out. The light intensities were both less than 1 LX. In addition, for underwater environments, turbidity is another important factor affecting the reconstruction quality. It has been shown that water becomes significantly turbid at 4 NTU and above [33]. For this reason, three test environments with turbidity levels of 2, 10, and 30 NTU were deployed, representing low turbidity, moderate turbidity, and high turbidity, respectively.

1) Reconstruction Results for Regular Shapes: In order to verify the reconstruction effect of the system for regular shapes, the plane circle, plane square, and cubic hemisphere are scanned and reconstructed, respectively. Fig. 15 shows the reconstruction results for three surfaces from low turbidity to high turbidity. After getting the point cloud of the object's surface, the plane and sphere are fit to the point cloud. The distance of each point from the fitting surface is calculated as the reconstruction error. The specific quantitative results are
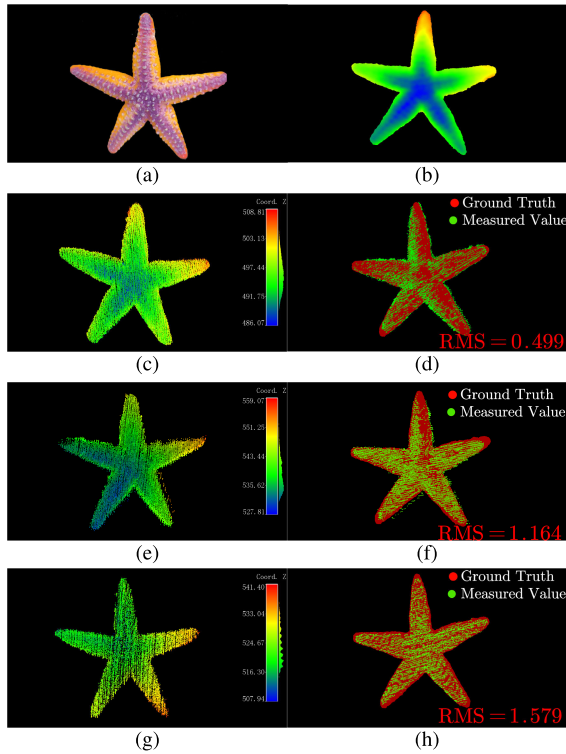
Fig. 16. Reconstruction results of starfish with different turbidity levels. (a) Picture of real starfish. (b) Ground truth by the depth camera. (c) Reconstruction result at low turbidity. (d) ICP result at low turbidity. (e) Reconstruction result at middle turbidity. (f) ICP result at middle turbidity. (g) Reconstruction result at high turbidity. (h) ICP result at high turbidity.

turbidity levels. The results are similar to the previous regular object reconstruction.

E. Discussion

According to the experimental results, our binocular structured light 3-D reconstruction system can measure objects of different materials and shapes at different distances with high accuracy in low-light underwater environments. In addition, excellent reconstruction results are achieved for both regular and irregular objects in different turbid waters. This is mainly attributed to the clever design, the accurate model, and the new laser-based calibration algorithm of the system proposed in this article.

It is obvious that, due to the severe light attenuation in water, it is difficult for a simple binocular camera to perform 3-D reconstruction underwater in low light [19], [22], [36]. Our system combines a binocular camera and laser to achieve high-accuracy measurement and reconstruction in turbid and low-light underwater. In addition, compared to the overall rotation of the system [26], [35], the galvanometer-based static scanning design is more suitable for robotic operation applications.

As can be seen in Table III, the accuracy of our refraction model measurements is much higher than that of the conventional triangular model (calibrated in air [32] or underwater [37]). This is because, when the system is placed to work in an underwater environment, the light penetrates through multiple layers of media and converges on the camera imaging plane. During this time, a significant refraction effect occurs.

Therefore, the light cannot simply be considered to travel along a straight line in this situation. Thus, the traditional limit constraint model is no longer valid. An underwater polar curve constraint model is proposed to ensure accurate matching of the laser points of the left and right cameras.

Currently, most underwater 3-D reconstruction systems' calibrations rely on a checkerboard [27], [28]. However, for underwater low-light environments, this checkerboard-based calibration method is difficult to use directly. Therefore, our proposed laser-based calibration algorithm is of great importance in low-light environments. As can be seen from Fig. 11, excellent calibration results are achieved even in environments less than 0.9 lx.

Of course, measurement errors inevitably exist. In the experiments, we found that it can be divided into three main categories. The first type of error is mainly generated by the system's own hardware. For example, the resolution of the camera affects the extraction of the pixel coordinates of the center of the laser line. Our method uses the gray centroid method to achieve subpixel extraction and mitigate its effect. The second type of error is mainly caused by the system measurement model and calibration errors. Our proposed method is significantly superior in this type of error. The third type of error is due to the external environment, which usually affects imaging quality and is the most significant source of error, including the turbidity of the water, the surface properties of the measured object, and so on.

At present, a lot of research work on underwater measurements and 3-D reconstruction is being carried out due to their importance for the operation of underwater robots. However, it is impossible to compare our system quantitatively with other research results due to the different principles, experimental environments, and so on. Therefore, we follow the comparison approach [22] and compare our system with the latest cutting-edge work, as shown in Table V. It is clear that our system has very high measurement and reconstruction accuracy, reaching the current state-of-the-art level. In addition, compared to other systems, our system is more robust to the environment and can operate in extreme underwater environments. Moreover, the system does not interfere with the robot's motion, which makes it more suitable for underwater robot applications, including underwater grasping, surveying, and mapping.

VII. CONCLUSION AND OUTLOOK

In this article, an underwater binocular structured light 3-D reconstruction system based on mirror galvanometer scanning is designed, which achieves high-accuracy static scanning reconstruction of underwater low-light scenes. On this basis, we systematically propose the underwater monocular imaging model and the binocular ranging model considering the refraction effect to improve the measurement accuracy. More importantly, the underwater binocular polar curve constraint model is proposed for the first time, which greatly improves the matching accuracy of laser stripe centerline. In addition, in order to better adapt to the underwater low-light environment, a simple calibration block with known width is designed,

and a new laser-based calibration algorithm based on action vision is proposed. The calibration task is transformed into a multiobjective optimization problem based on the geometric characteristics of the system laser. The proposed laser-based calibration algorithm only needs one scanning data, which greatly simplifies the calibration process. From the final experimental results, it is clear that our system has very high calibration, measurement, and reconstruction accuracy in a low-light environment, reaching the current state-of-the-art level.

At present, there is a relative lack of close-range high-precision 3-D reconstruction means for the underwater low-light environment, and our system will be expected to be applied to this special environment in the future, which can realize close-range 3-D perception of underwater robots for navigation, obstacle avoidance, grasping, and so on.

REFERENCES

[1] T. Salgado-Jimenez, J. L. Gonzalez-Lopez, L. F. Martinez-Soto, E. Olguin-Lopez, P. A. Resendiz-Gonzalez, and M. Bandala-Sanchez, "Deep water ROV design for the Mexican oil industry," in *Proc. OCEANS*, May 2010, pp. 1–6.

[2] M. Dunbabin, J. Roberts, K. Usher, G. Winstanley, and P. Corke, "A hybrid AUV design for shallow water reef navigation," in *Proc. IEEE Int. Conf. Robot. Autom.*, Apr. 2005, pp. 2105–2110.

[3] R. K. Katzschmann, J. DelPreto, R. MacCurdy, and D. Rus, "Exploration of underwater life with an acoustically controlled soft robotic fish," *Sci. Robot.*, vol. 3, no. 16, Mar. 2018.

[4] K.-T. Song, Y.-H. Chang, and J.-H. Chen, "3D vision for object grasp and obstacle avoidance of a collaborative robot," in *Proc. IEEE/ASME Int. Conf. Adv. Intell. Mechatronics (AIM)*, Jul. 2019, pp. 254–258.

[5] J. Shen and N. Gans, "Robot-to-human feedback and automatic object grasping using an RGB-D camera–projector system," *Robotica*, vol. 36, no. 2, pp. 241–260, 2018.

[6] C. Cadena et al., "Past, present, and future of simultaneous localization and mapping: Toward the robust-perception age," *IEEE Trans. Robot.*, vol. 32, no. 6, pp. 1309–1332, Dec. 2016.

[7] G. Bianco, A. Gallo, F. Bruno, and M. Muzzupappa, "A comparative analysis between active and passive techniques for underwater 3D reconstruction of close-range objects," *Sensors*, vol. 13, no. 8, pp. 11007–11031, Aug. 2013.

[8] A. Palomer, P. Ridao, and D. Ribas, "Multibeam 3D underwater SLAM with probabilistic registration," *Sensors*, vol. 16, no. 4, p. 560, 2016.

[9] A. Mallios, E. Vidal, R. Campos, and M. Carreras, "Underwater caves sonar data set," *Int. J. Robot. Res.*, vol. 36, no. 12, pp. 1247–1251, Oct. 2017.

[10] E. Westman and M. Kaess, "Wide aperture imaging sonar reconstruction using generative models," in *Proc. IEEE/RSJ Int. Conf. Intell. Robots Syst. (IROS)*, Nov. 2019, pp. 8067–8074.

[11] J. McConnell, J. D. Martin, and B. Englot, "Fusing concurrent orthogonal wide-aperture sonar images for dense underwater 3D reconstruction," in *Proc. IEEE/RSJ Int. Conf. Intell. Robots Syst. (IROS)*, Jan. 2021, pp. 1653–1660.

[12] S. Arnold and B. Wehbe, "Spatial acoustic projection for 3D imaging sonar reconstruction," in *Proc. Int. Conf. Robot. Autom. (ICRA)*, May 2022, pp. 3054–3060.

[13] E. Westman, I. Gkioulekas, and M. Kaess, "A theory of Fermat paths for 3D imaging sonar reconstruction," in *Proc. IEEE/RSJ Int. Conf. Intell. Robots Syst. (IROS)*, Jan. 2021, pp. 5082–5088.

[14] E. Westman, I. Gkioulekas, and M. Kaess, "A volumetric albedo framework for 3D imaging sonar reconstruction," in *Proc. IEEE Int. Conf. Robot. Autom. (ICRA)*, Aug. 2020, pp. 9645–9651.

[15] Y. Qian, Y. Zheng, M. Gong, and Y.-H. Yang, "Simultaneous 3D reconstruction for water surface and underwater scene," in *Proc. Eur. Conf. Comput. Vis. (ECCV)*, 2018, pp. 754–770.

[16] K. Ichimaru, Y. Taguchi, and H. Kawasaki, "Unified underwater Structure-from-Motion," in *Proc. Int. Conf. 3D Vis. (3DV)*, Sep. 2019, pp. 524–532.

[17] J. Xiong and W. Heidrich, "In-the-wild single camera 3D reconstruction through moving water surfaces," in *Proc. IEEE/CVF Int. Conf. Comput. Vis.*, Oct. 2021, pp. 12558–12567.

[18] K. A. Skinner and M. Johnson-Roberson, "Towards real-time underwater 3D reconstruction with plenoptic cameras," in *Proc. IEEE/RSJ Int. Conf. Intell. Robots Syst. (IROS)*, Oct. 2016, pp. 2014–2021.

[19] M. Johnson-Roberson et al., "High-resolution underwater robotic vision-based mapping and three-dimensional reconstruction for archaeology," *J. Field Robot.*, vol. 34, no. 4, pp. 625–643, Jun. 2017.

[20] K. A. Skinner, E. Iscar, and M. Johnson-Roberson, "Automatic color correction for 3D reconstruction of underwater scenes," in *Proc. IEEE Int. Conf. Robot. Autom. (ICRA)*, Jun. 2017, pp. 5140–5147.

[21] D. Berman, D. Levy, S. Avidan, and T. Treibitz, "Underwater single image color restoration using haze-lines and a new quantitative dataset," *IEEE Trans. Pattern Anal. Mach. Intell.*, vol. 43, no. 8, pp. 2822–2837, Aug. 2021.

[22] S. Kong, X. Fang, X. Chen, Z. Wu, and J. Yu, "A NSGA-II-based calibration algorithm for underwater binocular vision measurement system," *IEEE Trans. Instrum. Meas.*, vol. 69, no. 3, pp. 794–803, Mar. 2020.

[23] P. Risholm, T. Kirkhus, and J. T. Thielemann, "High-resolution structured light d sensor for autonomous underwater inspection," in *Proc. OCEANS*, Oct. 2018, pp. 1–5.

[24] J. Fan, X. Wang, C. Zhou, Y. Ou, F. Jing, and Z. Hou, "Development, calibration, and image processing of underwater structured light vision system: A survey," *IEEE Trans. Instrum. Meas.*, vol. 72, pp. 1–18, 2023.

[25] X. Wang et al., "An underwater structured light vision calibration method considering unknown refractive index based on Aquila optimizer," *IEEE Trans. Instrum. Meas.*, vol. 72, pp. 1–12, 2023.

[26] C. Gu, Y. Cong, and G. Sun, "Three birds, one stone: Unified laser-based 3-D reconstruction across different media," *IEEE Trans. Instrum. Meas.*, vol. 70, pp. 1–12, 2021.

[27] S. Chi, Z. Xie, and W. Chen, "A laser line auto-scanning system for underwater 3D reconstruction," *Sensors*, vol. 16, no. 9, p. 1534, Sep. 2016.

[28] A. Palomer, P. Ridao, J. Forest, and D. Ribas, "Underwater laser scanner: Ray-based model and calibration," *IEEE/ASME Trans. Mechatronics*, vol. 24, no. 5, pp. 1986–1997, Oct. 2019.

[29] M. Castillón, J. Forest, and P. Ridao, "Underwater 3D scanner to counteract refraction: Calibration and experimental results," *IEEE/ASME Trans. Mechatronics*, vol. 27, no. 6, pp. 4974–4982, Dec. 2022.

[30] A. Palomer, P. Ridao, D. Youakim, D. Ribas, J. Forest, and Y. Petillot, "3D laser scanner for underwater manipulation," *Sensors*, vol. 18, no. 4, p. 1086, Apr. 2018.

[31] A. Agrawal, S. Ramalingam, Y. Taguchi, and V. Chari, "A theory of multi-layer flat refractive geometry," in *Proc. IEEE Conf. Comput. Vis. Pattern Recognit.*, Jun. 2012, pp. 3346–3353.

[32] Z. Zhang, "A flexible new technique for camera calibration," *IEEE Trans. Pattern Anal. Mach. Intell.*, vol. 22, no. 11, pp. 1330–1334, Nov. 2000.

[33] *Water Quality and Health—Review of Turbidity: Information for Regulators and Water Suppliers*, World Health Org., Geneva, Switzerland, 2017.

[34] A. Anwer, S. S. A. Ali, A. Khan, and F. Mériaudeau, "Underwater 3-D scene reconstruction using Kinect V2 based on physical models for refraction and time of flight correction," *IEEE Access*, vol. 5, pp. 15960–15970, 2017.

[35] Q. Xue, Q. Sun, F. Wang, H. Bai, B. Yang, and Q. Li, "Underwater high-precision 3D reconstruction system based on rotating scanning," *Sensors*, vol. 21, no. 4, p. 1402, Feb. 2021.

[36] R. Detry et al., "Turbid-water subsea infrastructure 3D reconstruction with assisted stereo," in *Proc. OCEANS*, May 2018, pp. 1–6.

[37] A. Meline, J. Triboulet, and B. Jouvencel, "A camcorder for 3D underwater reconstruction of archeological objects," in *Proc. OCEANS*, Sep. 2010, pp. 1–9.

Yaming Ou received the B.E. degree in automation from Southeast University, Nanjing, China, in 2021. He is currently pursuing the Ph.D. degree in control theory and control engineering with the Institute of Automation, Chinese Academy of Sciences (IACAS), Beijing, China.

His research interests include underwater 3-D perception, simultaneous localization and mapping (SLAM), and robotic decision intelligence.

Junfeng Fan (Member, IEEE) received the B.S. degree in mechanical engineering and automation from the Beijing Institute of Technology, Beijing, China, in 2014, and the Ph.D. degree in control theory and control engineering from the Institute of Automation, Chinese Academy of Sciences (IACAS), Beijing, in 2019.

He is currently an Associate Professor of control theory and control engineering with the State Key Laboratory of Management and Control for Complex Systems, IACAS. His research interests include robot vision and underwater robots.

Chao Zhou (Member, IEEE) received the B.S. degree in automation from Southeast University, Nanjing, China, in 2003, and the Ph.D. degree in control theory and control engineering from the Institute of Automation, Chinese Academy of Sciences (IACAS), Beijing, China, in 2008.

He is currently a Professor of control theory and control engineering with the State Key Laboratory of Management and Control for Complex Systems, IACAS. His research interests include underwater robots and bionic robots.

Shifei Tian received the B.S. degree in automation from the North University of China (NUC), Taiyuan, China, in 2019. He is currently pursuing the M.S. degree in automation engineering with Northwestern Polytechnical University, Xi'an, China.

His current research interests include underwater binocular vision and deep learning.

Long Cheng (Senior Member, IEEE) received the B.S. degree in control engineering from Nankai University, Tianjin, China, in July 2004, and the Ph.D. degree in control theory and control engineering from the Institute of Automation, Chinese Academy of Sciences, Beijing, China, in July 2009.

He is currently a Full Professor with the Institute of Automation, Chinese Academy of Sciences. He is also an Adjunct Professor with the University of Chinese Academy of Sciences, Beijing. His current research interests include rehabilitation robots, intelligent control, and neural networks.

Dr. Cheng is also serving as an Associate Editor/Editorial Board Member of the IEEE TRANSACTIONS ON CYBERNETICS, *Neural Processing Letters*, *Neurocomputing*, *International Journal of Systems Science*, and *Acta Automatica Sinica*.

Min Tan received the B.E. degree from Tsinghua University, Beijing, China, in 1986, and the Ph.D. degree in control theory and control engineering from the Institute of Automation, Chinese Academy of Sciences, Beijing, in 1990.

He is currently a Professor with the State Key Laboratory of Management and Control for Complex Systems, Institute of Automation, Chinese Academy of Sciences. His research interests include advanced robot control, biomimetic robots, and multirobot systems.